A physics-based Antarctic melt detection technique: Combining AMSR-2, radiative transfer modeling, and firn modeling

Marissa E. Dattler[1,2,3], Brooke Medley[3], C. Max Stevens[2,3]

[1]Department of Atmospheric and Oceanic Sciences, University of Maryland, College Park, MD 20740, USA
5 [2]Earth System Science Interdisciplinary Center, University of Maryland, College Park, MD 20740, USA
[3]NASA Goddard Space Flight Center, Greenbelt, MD 20771, USA

Correspondence to: Marissa E. Dattler (marissa.e.dattler@nasa.gov)

Abstract. Surface melt on ice shelves has been linked to hydrofracture and subsequent ice shelf breakup. Since the 1990s, scientists have been using microwave radiometers to detect melt on ice shelves and ice sheets by applying various statistically

10 based thresholds to identify significant increases in brightness temperature that are associated with melt. We combine a statistical thresholding technique with Community Firn Model outputs, the Snow Microwave Radiative Transfer model, and AMSR-2 to create a hybrid method that accounts for the influence of variations in snow temperature and density on microwave brightness temperature. In the process, we also produce snow correlation lengths, and we run this algorithm on 13 sites over the Antarctic Ice Sheet and ice shelves. Compared to melt values from surface energy balance observations from automatic

15 weather stations, this method is as accurate as previous statistically based thresholding techniques and is slightly more sensitive to melt events. Our correlation lengths from early 2014 correlate with surface grain size from the 2013-2014 Mosaic of Antarctica. We also find a significant relationship between correlation length and frequency of melt. In the future, this hybrid method can be further developed to quantify melt volume rather than to simply detect melt occurrence.

1 Introduction

20

Studying Antarctic surface melt is critical for evaluating the relationship between the AIS and the climate system. Climate change has been associated with increased surface melt and pond formation in Antarctica, particularly in the Antarctic Peninsula (Scambos et al., 2000). While only a small percentage of surface meltwater runs off into the ocean, recent studies have shown that meltwater on the surface of ice shelves can lead to hydrofracture and ice shelf collapse (Scambos et al., 2000;

25 Banwell et al., 2013; Kingslake et al., 2017; Bell et al., 2018). Since ice shelves provide a buttressing effect to ice upstream, their collapse can indirectly contribute to mass loss of the Antarctic Ice Sheet (AIS) through increased ice discharge into the ocean contributing to sea level change (Rignot, 2004; Berthier et al., 2012).

To identify surface melt on the AIS from passive microwave radiometry, previous studies have used a variety of statistical

30 techniques that detect spikes in brightness temperature above a predetermined threshold, which are interpreted as melt events (Zwally and Fiegles, 1994; Torinesi et al., 2003; Picard et al., 2007). Typically, the threshold remains temporally constant over

a year or longer and is based on mean brightness temperature for the 18 to 19 GHz frequency in the horizontal polarization. If the brightness temperature exceeds this threshold on a given day, then that day is assigned to be a melt day. However, variations in brightness temperature can also occur due to changes in snow density, physical temperature, and microstructure. These

35 thresholding techniques that have been developed to detect surface melt on the AIS have not generally considered these physical properties of the snow. In part, this omission is because the properties of snow over the AIS are not well known. However, recent improvements in atmospheric reanalysis, firn modelling, and snow radiative transfer modelling allow us to create a hybridized physics-based technique for detecting melt.

40 In this study, we address the need for a microwave melt-detection technique that has a physical basis in the complex dynamics of snow microwave radiation. To achieve this, we create a dynamic threshold that captures the microwave effects of snow-property variability from day to day, instead of a statistically based threshold that only varies year to year. Our new, dynamic thresholding technique identifies melt days while quantifying the effects of snow temperature and density on brightness temperature. First, we use inverse radiative transfer modelling to determine snow microstructure (correlation length) using the

45 Community Firn Model and the Snow Microwave Radiative Transfer model. Then, we use the outputs of these models to compute daily-varying thresholds. When a daily threshold is exceeded by AMSR-2, we mark it as a melt day. We analyze our melt detection results from our hybrid, physics-based technique by comparing our results to Antarctic Weather Station (AWS) data as well as results from statistically based techniques. We analyze the frequency at which we detect melt days, as well as our intermediary calculations of snow microstructure, at thirteen sites in Antarctica.

2 Data & Models

2.1 AIS point weather observations

We analyze near-surface observations from ten AWS; we selected these sites due to their hourly melt rates from surface energy balance (SEB) analysis based on observed conditions (Jakobs et al., 2020). These hourly melt rates are converted to daily melt rates for comparison to microwave data. We use three additional dry sites that were added for comparison; these sites are

55 Dome C (DC; 75.10ºS, 123.35ºE), Point Barnola (PB; 75.70ºS, 123.25ºE), and Kohnen (75.00ºS, 0.07ºE). The locations of all sites are shown in the map in Figure 1. These AWS are found on grounded ice sheet, ice shelves, or ice rises as shown in Figure 1 (Jakobs et al., 2020). Our time series spans at least from the beginning of 2014 to the end of 2018 for all sites. We use longer records from AWS 17 (2012-07-02 to 2019-05-31) and AWS 18 (2014-01-01 to 2019-05-31) for a longer comparison with SEB-derived melt data for these two sites. Our analysis of AWS 17 starts in 2012-07-02 and ends 2019-05-31, and AWS 18

60 starts on 2014-01-01 and ends 2019-05-31.

2.2 Advanced Microwave Scanning Radiometer 2 (AMSR-2)

AMSR-2 is a microwave radiometer onboard Japanese satellite Global Change Observation Mission – Water Satellite 1 (GCOM-W1). This instrument provides 16 channels between 6.9 and 89 GHz. We use the 18.7 GHz channel, as this frequency is most sensitive to the presence of liquid water on the surface of the Antarctic Ice Sheet. Tikhonov et al. (2019) showed that the penetration depth of 19 GHz was a few tens of centimeters using the Special Sensor Microwave/Imager (SSM/I) passive microwave radiometer. We use the 12.5 km x 12.5 km daily gridded product of AMSR-2.

2.3 Community Firn Model

The Community Firn Model (CFM) is an open-source model framework that simulates firn property evolution, including densification, temperature, melt, and grain growth (Stevens et al., 2020). Because surface grain size over the Antarctic Ice Sheet is not well constrained, the grain growth model for dry snow within CFM assumes a fresh snow grain radius of 0.1 mm across the Antarctic Ice Sheet (Stevens et al., 2020). When compared to surface grain sizes derived from the Mosaic of Antarctica, this is an underestimate for many areas of the AIS associated with frequent melt events, especially ice shelves (Scambos et al., 2007). We force the CFM with daily Modern-Era Retrospective analysis for Research and Applications, Version 2 (MERRA-2) precipitation and skin temperature (Gelaro et al., 2017). The CFM output is on the same spatial resolution as MERRA-2: 0.5º latitude by 0.625º longitude (Gelaro et al., 2017). The vertical resolution of the daily output profiles from the CFM varies spatiotemporally, and, generally, is too fine for input into the radiative transfer model. To a significant degree, the more layers that are input into the radiative transfer model, the more computationally expensive it is to model snow brightness temperature. Therefore, we merge thin layers from the CFM output to create thicker layers that are appropriate for the sensitivity of AMSR-2 at the 18.7 GHz frequency. From the surface down to 1 m, each layer is approximately 1 cm in thickness. From 1 m to 5 m, each layer is approximately 10 cm. A single, semi-infinite bottom layer spans 5 m to 50 m. The exact size of each layer varies slightly from day to day and location to location due to layer formation and merging within the CFM. The CFM output we use has daily temporal resolution.

2.3 Snow Microwave Radiative Transfer model framework

The Snow Microwave Radiative Transfer (SMRT) framework simulates thermal emission and backscattering while allowing for the use of several previously developed microstructure and scattering models, including the Dense Media Radiative Transfer model (DMRT) and the Improved Born Approximation (IBA; Picard et al., 2018). These two models are shown to produce nearly equivalent results (Löwe and Picard, 2015). We choose to implement the IBA within SMRT because it considers snow microstructure as a single parameter (Picard et al., 2018)

90

3

3 Methodology

We use the radiative transfer model SMRT to predict brightness temperatures based on each day's modeled snow conditions. Snow temperature, density, correlation length, and liquid water volume all affect snow brightness temperature and are inputs into SMRT. We always set the snow's liquid water volume to zero regardless of how much liquid water is truly present that
95   day. In doing so, we compute dry-snow brightness temperatures, which are lower than the brightness temperatures that occur when snow is wet. In theory, our modeled dry snow brightness temperatures should equal observed brightness temperatures on days with no liquid water present. We consider melt to have occurred on a given day when the observed brightness temperature from AMSR-2 exceeds the modeled dry-snow brightness temperature by at least a fixed amount.

100 We input snow density and temperature from the CFM into SMRT. Snow microstructural parameters are also required for snow radiative transfer modeling, specifically correlation length for SMRT-IBA. However, accurate, daily-varying correlation lengths are not currently available across the AIS either from modeling or remote sensing. The CFM produces vertical grain size profiles, which can be converted to correlation length with some uncertainty; however, these profiles from CFM are highly dependent on fresh snow grain size, which is not currently well enough known across the AIS for use in microwave studies.
105 Instead, we first use snow brightness temperature to determine snow microstructure, specifically correlation length, on days that we are confident that the snow is dry.

We can make this determination because brightness temperature for 18.7 GHz in both the horizontal and vertical polarizations (18H and 18V, respectively) decreases considerably as a function of correlation length (Figure 2a). Overall, the brightness
110 temperature is more sensitive to correlation length than to temperature or density (Figures 2b and 2c). Thus, using accurate correlation length values to determine brightness temperature is important. Instead of inputting correlation length from an outside source, we first solve for correlation length on dry days when correlation length is the only SMRT input variable that is unknown.

115 In this study, we focus our melt detection analysis on the horizontal polarization as it has been shown to be sensitive to the presence of liquid water on the surface of the AIS, making it useful for melt detection (Zwally and Fiegles, 1994 and Torinesi et al., 2003). However, the vertical polarization can also be useful specifically in microwave radiative transfer modelling as it is generally easier to model the vertical component of emissivity than the horizontal component. This is because the vertical component of emissivity is not as sensitive to the detailed density structure of icy layers (Comiso et al., 1997; Durand et al.,
120 2008). Therefore, we run the following steps for both the 18H and 18V channels for each of the sites.

3.1 Calculating correlation length (p_{exp}) for potential dry days

Our goal is to calculate correlation length based on brightness temperature observed by AMSR-2 on dry days. Note that we have not assigned melt days at this point in the process because we have not yet created our dynamic threshold. Instead, we

125 identify "potential melt days" as any day within +/- 7 days of a melt day detected by the thresholding technique described in Picard et al. (2022a). "Potential dry days" are outside this +/- 7-day window. We chose the threshold from Picard et al. (2022a) over other statistical techniques because it uses a threshold of only 20 K above the mean, horizontally polarized brightness temperature of its assigned dry season (June to September), typically making it most sensitive to melt resulting in more "potential melt days" than other statistically based thresholding techniques.

130

SMRT predicts brightness temperature based on input snow conditions. We employ what is termed "inverse radiative transfer modeling". This technique was used in Picard et al. (2012) to calculate grain size for Dome C. Unlike Picard et al. (2012), we use a shorter, single frequency (18.7 GHz) and assume vertically homogenous snow microstructure. One way to employ inverse radiative transfer modeling for these two polarizations is to run the radiative transfer model for a range of monotonically

135 increasing input correlation lengths and then select the correlation length that produces a modeled brightness temperature closest to the observed brightness temperature. In our methodology, we apply a slightly different process that yields equivalent results but is optimized for computational efficiency.

In our process, for a potential dry day, we run SMRT once with an overestimate or a "high" value for correlation length and a

140 second time with an underestimate or a "low" value for correlation length. We assume temperature and density profiles based on CFM outputs. This results in both an overestimate and an underestimate for brightness temperature, as brightness temperature decreases as a function of correlation length at this frequency. Using these two endmembers as bounds, we linearly interpolate to the observed brightness temperature to find a correlation length associated with this value. We repeat this process many times over with more accurate correlation lengths with narrower bounds. Eventually, we converge on a correlation length

145 for that day that, when input into SMRT, produces a modeled brightness temperature that is approximately equal to the observed brightness temperature.

To invert this radiative transfer model, we run an algorithm with three separate processes: Process 1, Process 2, and Process 3, which are illustrated in Figure 3. The goal of Process 1 is to make a general initial estimate for correlation length for that

150 location. The goal of Process 2 is to use that estimate to determine how correlation length varies approximately month to month. Since Processes 1 and 2 are only in place for optimizing computational efficiency, we only consider the steps in Figure 3a to 3d one time through for each of these two processes. Finally, in Process 3, we converge on a correlation length that, when input into SMRT with CFM input temperature and density, best matches the local observed brightness temperature.

155 For Process 1, we establish two correlation length scenarios in Figure 3b for one, single potential dry day. For the two different scenarios, we assume a higher bound (p_{high}) and lower bound (p_{low}) for correlation length while assuming the same CFM temperature and density profiles for both scenarios. We determine these two values by consulting the table in Figure 3b*. For this single day, $p_{initial}$ is set to 0.3 mm with a +/- 0.2 mm bound. Thus, in Figure 3c, we run two instances of SMRT with

160 correlation length values of 0.1 mm and 0.5 mm. This produces two brightness temperatures, T_{B1} and T_{B2}. We linearly interpolate between the points (p_{low}, T_{B1}) and (p_{high}, T_{B2}) to the AMSR-2 brightness temperature observed that day. This results in an approximated correlation length, p, for this location. This marks the completion of Process 1.

Next, we perform Process 2, which consists of running every twentieth potential dry day. For each of these days, instead of setting $p_{initial}$ to 0.3 mm, we set $p_{initial}$ to the single p from Process 1. We also use a slightly smaller bound of +/- 0.05 mm, in
165 accordance with the table in Figure 3b*. We complete the steps outlined in Figure 3a through 3d, running SMRT twice and linearly interpolating to the observed brightness temperature from AMSR-2. This results in a new approximation, p, for every twenty days of the time series. We linearly interpolate across the time series to find an approximate correlation length, p, for every day in the time series. This marks the completion of Process 2.

170 For Process 3, for every day in the time series, we now consider the full loop of the algorithm outlined in the flow chart. For potential dry days, we start with a $p_{initial}$ based on our results for p from the corresponding day in Process 2. We start with bounds from the table in Figure 3b*; our first bounds are thus $p_{initial}$ +/- 0.01 mm. Again, running SMRT twice with these two correlation length bounds, we find two brightness temperatures associated with these bounds. Interpolating between those brightness temperatures to the observed brightness temperature, we find a correlation length, p. Then, we input p in SMRT,
175 along with CFM temperature and density profiles for that day, to find a modeled brightness temperature associated with that correlation length. In Figure 3e, we compare this value to the AMSR-2 brightness temperature; if the two values are not within 0.01 K, then $p_{initial}$ is set to p and we proceed to Figure 3b. We repeat this process, with smaller and smaller bounds according to the table in Figure 3b*.

180 This minimization results in modelled correlation lengths during potential dry days that, when input into SMRT along with temperature and density from CFM, each produce a brightness temperature that is within 0.01 K of its respective AMSR-2 observation. Note that we would have found equivalent results by simply following the full algorithm depicted in the flow chart without breaking steps into Processes 1 through 3. We only separated out the processes so that we could initially find general estimates of correlation length on fewer days instead of running it on every single potential dry day, thus decreasing
185 the code's runtime.

3.2 Assigning melt days and dry days

After we have established correlation lengths for each of the potential dry days, we consider correlation length on potential melt days. Since melt dramatically increases brightness temperature, we cannot compute correlation length during potential
190 melt days using the method described in Section 3.1. In the absence of other information, we determine the correlation length on potential melt days by linearly interpolating between the non-melt days (Figure 3f). This results in our final correlation lengths, p_{exp}, every day across the time series.

Now that we have a correlation length product, we can calculate brightness temperatures under the assumption that every day

195 is dry. To do this, we use the temperature and density profiles from CFM for each day as inputs for SMRT. This generates dry snow brightness temperatures, $T_{B,dry\ snow}$, as seen in Figure 3g. To calculate our threshold brightness temperature, we subtract a fixed value from correlation length. For this, we use the four-fold mean of a 31-day windowed running standard deviation of correlation length along our time series for potential dry days (hereafter referred to as $4\overline{\sigma_{p_{exp}}}$). We chose $4\overline{\sigma_{p_{exp}}}$ because our temporal linear interpolation across the potential melt days would yield a poorer estimation of correlation length for locations

200 where correlation length is varying significantly from day to day. As shown in Figure 3g, we input this lower bound on correlation length into SMRT along with the CFM temperature and density information to generate a dynamic threshold, $T_{B,threshold}$, that varies from day to day. The presence of liquid water causes an increase in brightness temperature; we interpret any day where the AMSR-2 brightness temperature exceeds this dynamic threshold as a melt day and any day that falls below as a non-melt day, or a dry day. This is shown in Figure 3h. We call this the hybrid method.

205

4 Results

4.1 Dry-snow zone: Validation

The purpose of this study is to detect the presence of liquid water in a more physically based way and assess the technique's usefulness in detecting melt. Before applying our dynamic thresholding method to determine melt days, we test how AMSR-

210 2, SMRT, and CFM can be used together to estimate brightness temperature at a dry site. We use Dome C, a cold site on the Antarctic Plateau, as our test site. Figure 4a shows that the brightness temperature in 18H never exceeds the Picard et al. (2022a) threshold, so, by default, 0% of the time series would be considered to have melt according to the hybrid method as we detect no potential melt days.

215 As seen in Figure 4b, the correlation length has a mean of 0.20 mm for 18V and appears to have a seasonal signal; higher correlation lengths occur during the austral winter, and lower correlation lengths occur during the austral summer. The amplitude of this oscillation is about 0.015 mm, or 7.5% of the mean correlation length for this site. Since the CFM-modeled snow and firn temperature is influenced by MERRA-2 skin-temperature forcing, we compare the MERRA-2 skin temperature to in situ temperature data from Dome C to check for a seasonal bias. Indeed, there is a seasonal bias in the MERRA-2 skin

220 temperature for this site, and we remove it using a linear regression. We re-run the CFM with the bias-corrected (BC) temperature input and we recalculate correlation length using SMRT. Figure 4b shows that the correlation length no longer varies seasonally after our bias correction. The correlation length also increased in the BC run by a mean of about 10%.

We compare our correlation lengths to a snow profile with Specific Surface Area (SSA) measurements at Dome C (Picard et

225 al., 2022b). We convert SSA to an exponential correlation length profile following the relationship described in Mätzler (2002). We compare our SMRT-derived correlation lengths to two profiles located at Dome C that are approximately 7 m in depth.

We would not expect an exact match for this comparison because (a) correlation length varies within the 12.5 km AMSR-2 grid cell and (b) the penetration depth of AMSR-2 is approximately 4 to 10 m, meaning its brightness temperature is likely sensitive to snow deeper than the 7 m profile. Despite these factors, all of the in situ- and SMRT-derived correlation lengths

230 fall in the 0.185 mm and 0.225 mm range (Figure 4b).

Our results show that neither the dry-snow brightness temperatures nor our dynamic threshold are significantly affected by the bias correction. Though the bias correction does result in about a 10% change in correlation length for Dome C, this correction does not significantly impact the dry snow brightness temperature nor our dynamic threshold. In fact, if we displayed them in

235 the same panel for comparison they would almost completely overlap; therefore, we show them separately in Figure 4c and 4d. The difference between the two is shown in Figure 3e with the maximum absolute difference of less than 0.02 K. This value is less than the radiometric resolution of the instrument (Maeda et al., 2015), showing the robustness of these methods despite errors in MERRA-2. We also compare the BC and non-BC dynamic thresholds, shown in Figure 4c and 4d. Seen in Figure 4f, the maximum absolute difference is 0.35 K, less than 1% of a realistic brightness temperature for an ice sheet or ice

240 shelf at this channel. Since the errors propagated into our dynamic threshold are low, we are satisfied with using the non-BC temperature forcing. However, we acknowledge that there may be biases in correlation length as all errors in temperature and density are propagated there. The corresponding results for 18H instead of 18V are similar and can be found in the Supplemental Materials.

245 **4.2 Melt-zone test sites: Comparison to SEB-derived melt data**

Now that we have established the feasibility of using SMRT and CFM to model Antarctic brightness temperatures, we branch out to sites that experience seasonal melt. We focus on two sites: AWS 18 on the Larsen C ice shelf and AWS 17 on a remnant of the Larsen B Ice Shelf (Figure 1). We chose these two sites as the SEB observations overlap with AMSR-2 observations over several years. Unless otherwise stated, the results we present use the 18H AMSR-2 channel due to its sensitivity to melt.

250 For both AWS 17 and AWS 18, there are days where AMSR-2 brightness temperature exceeds the thresholds from Zwally and Fiegles (1994), Torinesi et al. (2003), and Picard et al. (2022a) each year, seen in Figures 5a and 6a. The hybrid method can detect extra days of melting occurring within a 15-day window of a particular melt day identified by Picard et al. (2022a). Given the numerous occasions where AMSR-2 brightness temperatures surpass the Picard et al. (2022a) threshold each year, there are a substantial number of days that the hybrid method could classify as melt. To quantify this number of days, we first

255 consider the correlation length at each site.

For AWS 17, the mean correlation length is 0.47 mm, shown in Figure 5b. The linearly interpolated correlation length increases across each of the four austral summers shown, suggesting grain growth due to wet snow metamorphosis (Brun, 1989). In Figure 5c, the dry snow brightness temperature lines up exactly with the AMSR-2 brightness temperature because of how we

260 calculated the correlation length during all potential dry days. The propagated $4\overline{\sigma_{p_{exp}}}$ thresholding bound we use to determine

melt days varies from about 155 K to 185 K across this time series. Melt days make up 24% of the time series using the hybrid method and 21% of the time series according to SEB-derived melt data. In Figure 5d, melt days and dry days that are assigned by the hybrid technique match with SEB-derived melt rates for 90.9% of the time series, which is second best of the techniques we studied. The Picard et al. (2022a) thresholding technique matches SEB-derived melt rates best for this location at 91.7%

265   (Table 1).

The results for AWS 18 are similar to AWS 17; AMSR-2 brightness temperature gain exceeds all three statistical thresholds annually, shown in Figure 6a. The mean correlation length is 0.38 mm. As in AWS 17, the interpolated correlation lengths for AWS 18 increase over each of the four austral summers shown in Figure 6b, again indicating increased grain growth due to

270   wet snow metamorphosis. The dry snow brightness temperature matches the AMSR-2 brightness temperature during all potential dry days, shown in Figure 6c. The propagated $4\overline{\sigma_{p_{exp}}}$ thresholding bound we use to determine melt days is higher than that of AWS 17, and it varies from about 170 K to 210 K across this time series. In Figure 6d, melt days from our hybrid technique match SEB-derived melt data between melt days and dry days for 90.9% of the time series.

275   For AWS 17 and 18, in Figures 7a and 7c, respectively, we can see that our dynamic threshold is generally at equal or lower values than the Picard et al. (2022a) threshold. The SEB-derived melt data indicate occasional melt events during the austral winter that are not picked up by the hybrid method or any of the three statistical thresholding methods. Generally, for both sites, the hybrid method marks melt more frequently than the three statistical measures. Among the four techniques, the hybrid method selects melt the largest percentage of the time, at 28% of the days of the over 5-year time series for AWS 18, as

280   compared to the SEB-derived melt data which indicate melt 27% of the time, both shown in Table 1.

Comparing the three statistical methods to our hybrid method in Table 1, we can see the hybrid method is most likely to assign melt days compared to Picard et al. (2022a), Torinesi et al. (2003), and Zwally and Fiegles (1994), in decreasing order. At AWS 18, the melt season is generally longer than AWS 17. The percentage of melt days in AWS 17 and 18 was higher than

285   that of the SEB-derived melt data by 3.5% and 0.6%, respectively, as seen in Table 1. However, the Picard et al. (2022a) melt days matched with the SEB-derived melt data for the greatest percentage of the time series for both sites, with the hybrid technique following at the next highest rate.

4.3 All sites: Frequency of melt and correlation length

290   Aside from AWS 17 and 18, none of the other sites have both (a) significant amount of crossover in time with AMSR-2 and SEB observations and (b) frequent melt. Therefore, we cannot compare their results to SEB-derived melt data. Instead, we compare the melt-detection data derived from the hybrid method to other statistically based techniques. In Figure 8a, we can see that no melt days were detected in the dry snow zone of Wilkes Land. Likewise, no melt was detected over AWS16 in Dronning Maud Land. Kohnen, AWS 5, and 6 were the only sites located on grounded ice sheet that were found to have any

295   melt days by any of the four detection methods. For AWS 5, the hybrid method in the horizontal polarization detected almost double the number of melt days that were detected by Picard et al. (2022a). Ice shelves in the Dronning Maud Land region had significantly more melt than over the grounded ice sheet, as detected by the hybrid method and all four statistically based thresholding techniques. The sites found on the Antarctic Peninsula ice shelves had about double the number of melt days as those on Dronning Maud Land ice shelves, irrespective of the chosen thresholding technique. For most of the sites, the hybrid

300   method in both horizontal and vertical polarizations detected more melt days than the other three techniques. The closest behind is the Picard et al. (2022a) method.

In addition to melt frequency, correlation length varies from location to location, as we can see in Figure 8b. Among these thirteen sites, lower correlation lengths are found on grounded ice sheet. Slightly higher correlation lengths are found on the

305   ice shelves of Dronning Maud Land. Correlation lengths are highest at the Antarctic Peninsula, for the Larsen B ice shelf remnant site, and the three Larsen C sites. This is a similar pattern to frequency of melt days. The correlation length using the horizontal polarization is consistently slightly higher than that of the vertical polarization. In Figures 8c and 8d, we compare our correlation lengths to grain size from the 2014 NASA Making Earth System Data Records for Use in Research Environments (MEaSUREs) MODIS Mosaic of Antarctica (MOA) (Scambos et al., 2007; Haran et al., 2018). Our

310   corresponding correlation lengths using the vertical polarization are correlated with MOA optical grain radius at a r^2 of 0.75 ($p < 0.01$) in Figure 8c. In Figure 8d, using 18H, MOA optical grain radius is correlated to correlation length at a slightly lower r^2 of 0.64 ($p < 0.01$).

We can see strong seasonal variations in correlation length for all sites that experience melt using both horizontal (Figure 9a)

315   and vertical polarizations (Figure 9b). The sites appear to divide into two groups: sites with greater or less than 5% melt days (or about 18 melt days per year). Sites with greater than 5% melt day frequency tend to have, on average, about 0.2 mm higher correlation length than sites with less than 5% melt day frequency. Comparing Figure 9a to 9b, the horizontal polarization shows higher variability in correlation length for each site as well as a larger range in correlation lengths from site to site. For sites with nonzero melt (according to the hybrid method), mean correlation length correlates with the percentage of melt days

320   at an r^2 of 0.75 ($p < 0.01$) and 0.81 ($p < 0.01$) for 18H and 18V, respectively; there appears to be a strong relationship between correlation length and the frequency of melt days. For further information, melt detection figures for all thirteen sites for both 18H and 18V are provided in the Supplemental Materials.

5 Discussion

325   The hybrid method has both benefits and drawbacks when we compare it to statistical thresholding techniques. At present, the hybrid method is tied to a statistical thresholding technique described in Picard et al. (2022a); our method limits the potential days that could be assigned melt to a 15-day window around days that are considered melt by Picard et al. (2022a). While this allows our method to detect melt days that are clustered close to melt events detected by Picard et al. (2022a), it also prevents

The Cryosphere
Discussions

our method from detecting any melt events that are isolated in time, such as over the austral winter. However, future work may

330 allow for this method to be independent from statistical thresholding. For example, future work could include making the potential melt days self-consistent with the calculated melt days in an iterative fashion. This method would then be able to identify some small or localized melt events that are isolated in time from larger melt events that are detected by statistical thresholding. Additionally, we acknowledge that, though our dry snow brightness temperatures are physics-based, our fixed bound on correlation length ($-4\overline{\sigma_{p_{exp}}}$) to calculate the dynamic threshold is based in statistics. Improvements in firn modeling,

335 especially of snow microstructure, would allow us to more accurately model dry snow brightness temperature and allow us to reduce this bound on correlation length.

For two sites on the Antarctic Peninsula, we discovered that the hybrid method does not necessarily improve the agreement between melt events determined by SEB-derived melt data and melt events predicted by the hybrid method. However, it is

340 important to note that this may specifically be because we are comparing our method to the Picard et al. (2022a) technique for only two locations. In Picard et al. (2022a), they focused on the sensitivity of microwave brightness temperature to total liquid water content rather than melt detection. Therefore, their goal in melt detection was "simplicity and reproducibility" for eight sites rather than designing the most physical and robust algorithm for meltwater detection across the AIS (Picard et al., 2022a). However, the eight sites used in the Picard et al. (2022a) method have crossover with the two sites we evaluated in comparison

345 to SEB-observations. Picard et al. (2022a) also used AWS 17 on Larsen B and used AWS 15, which is near to AWS 18.

It would have been ideal for us to test our method on fresh sites that have not been used to create melt detection algorithms, but we are limited to sites that have significantly long SEB observations so we can validate our melt detection technique. However, since our method is adapted to the conditions of the snow and firn, we expect our algorithm to be robust to changes

350 in temperature and density variations from time to time and location to location. To note, the reason why we chose the Picard et al. (2022a) method for hybridization is not because it is always the optimal method for melt detection (by itself) across the AIS, but because its relatively small +20 K fixed threshold results in the highest number of potential melt days than the other statistically based thresholding techniques. This allows for the most flexibility for the hybrid method, as there are more "potential melt days" allowable for the hybrid method to sort into melt and dry days.

355

Another key difference between the hybrid method and statistical thresholding techniques is that the hybrid method provides correlation length, an additional piece of information that may be useful in multiple ways. In our comparison of the hybrid method's correlation lengths to optical grain radius from MOA, we see a significant relationship between these two values. This relationship is especially strong for the 18V channel. Although the 18H channel is a good choice for melt detection, as it

360 is very sensitive to the presence of liquid water, it is generally easier to model snow brightness temperature accurately for the vertical polarization, as discussed in the methods section. This is because the horizontal component of emissivity can be reduced significantly by icy layers, which may not be fully captured in CFM or modeled within SMRT (Comiso et al., 1997;

Durand et al., 2008). The resulting overestimate of emissivity may result in an overestimate of correlation length to compensate. This is most likely why vertically derived correlation lengths are generally lower than horizontally derived

365 correlation lengths, and why vertically derived correlation lengths show a higher correlation with MOA. However, we do not expect a one-to-one correlation to MOA using either of these polarizations. This is primarily because the 18.7 GHz frequency is sensitive to the upper 5 to 10 m of snow, whereas MODIS is predominantly sensitive to the first 1 cm of snow (Lyapustin et al., 2009).

370 Additionally, we do not expect melt from SEB-derived melt data to agree exactly with melt days detected by a spaceborne microwave radiometer. One reason is that SEB-derived melt data deduce the melt volume produced on a certain day, whereas a "melt day" indicates the presence of liquid water on the ice sheet as derived from daily microwave data. While we expect these two variables to be very well correlated, we do not expect them to match exactly because liquid water can persist on the surface of the ice sheet even though the snow is not actively melting. Furthermore, since melt may not always occur during

375 overpasses, AMSR-2 may miss or preferentially detect melt. Differences can also result from the large footprint of the microwave radiometer. The hybrid method may be more sensitive to smaller jumps in brightness temperature that may be associated with localized melt events that are nearly averaged out by the 12.5 x 12.5 km footprint of AMSR-2.

This study also revealed a significant correlation between percentage of melt days and the correlation length of that site. Any

380 error in the CFM's temperature and density information could theoretically propagate into the following four parameters: correlation length, dry snow brightness temperature, our dynamic threshold, and number of melt days, as illustrated by the flow chart in Figure 3. However, that alone would not necessarily lead to a positive correlation between the hybrid method's correlation length and the number of melt days assigned by the hybrid method.

385 To illustrate the propagation of these biases, we describe an example scenario where MERRA-2 has biased-high skin temperature for a particular site. Then CFM would have a biased-high snow temperature profile. We solve for correlation lengths on dry days that, along with CFM density and biased-high temperature profiles, result in modeled dry snow brightness temperatures that match AMSR-2. Correlation length will be overestimated, contributing to a reduction in dry snow brightness temperature to compensate for the artificial increase caused by the biased-high temperature profile. Dry snow brightness

390 temperature on dry days is, by definition, robust to errors in MERRA-2 because it is forced to match AMSR-2. However, overestimating correlation length which may mean also overestimating the standard deviation in correlation length which will result in a biased-high dynamic threshold and fewer detected melt days. The reverse would be true for underestimating MERRA-2 skin temperature. SMRT input biases would act to reduce the correlation between correlation length and frequency of melt days.

395

This relationship between correlation length and frequency of melt days is likely to be physical in nature. It suggests that the snow microstructure is related to the percentage of the year in which snow undergoes melt. This relationship has a physical basis; wet snow metamorphism leads to faster grain growth than dry snow metamorphism (Brun, 1989), which is likely why locations that experience significant melt tend to have higher correlation lengths. These variations in correlation length and

400   snow texture are important because they affect the thermal conductivity, permeability, dielectric properties, and optical properties of snow. Therefore, correlation length is highly relevant for ice sheet research, especially satellite altimetry, as snow microstructure influences radar penetration depth.

The ultimate reason for this study is to build on melt detection research with the goal of melt quantification across the Antarctic

405   Ice Sheet. Currently, observations of melt quantity in Antarctica are limited to a small number of in-situ surface energy balance sites. In this study, we show the feasibility of using a satellite- and physics- based approach to melt detection. With additional refinement and calibration, this hybrid method has potential to estimate melt volumes instead of simply detecting the presence of melt. In a similar way to how we used inverse radiative transfer modeling to calculate correlation length, we could potentially use it to solve for melt volume. An algorithm that solves for even a rough estimate of melt volume would constitute a key step

410   forward in understanding surface melt across the Antarctic Ice Sheet. This improvement would likely require the use of multiple frequencies and polarizations. This inverse problem is especially complex because liquid water has varying stratification vertically. More testing would need to be done to not only see what volume and vertical distribution of melt would saturate the microwave signal at a given frequency, but also understand the effects of localized melt within the 12.5 km AMSR-2 footprint. Quantifying surface melt from microwave radiometry is a complex problem; however, addressing it would

415   greatly improve our understanding of surface melt on ice sheets and ice shelves.

6 Conclusions

Using the hybrid method, we can estimate the correlation length of snow by combining firn-model outputs and inverse radiative transfer modeling forced by AMSR-2 for dry-snow conditions. Next, we show how to interpolate the correlation length across

420   the melt season, using it along with information from CFM to forward model brightness temperature assuming dry snow conditions. This approach allows us to create a dynamic, hybrid threshold to identify melt days in a way that addresses day-to-day fluctuations in weather and snow conditions. Bias correction of reanalysis forcing can affect modeled correlation length but only minorly influences the dry-snow brightness temperature. Examining ice shelf sites on the Antarctic Peninsula and comparing to SEB-derived melt data, we find that the hybrid method performs similarly to the thresholding techniques.

425   However, it generally flags a greater number of days as melt days. The hybrid technique has the advantage of providing additional information useful for radar studies, such as correlation length. This work shows that we can combine firn modeling with radiative transfer modeling to determine properties of the snow, potentially expanding the use of snow radiative transfer modeling beyond point locations with observational data. This methodology can be further developed for use in melt volume studies, as opposed to simply melt detection.

The Cryosphere
Discussions

Author Contributions

MD and BM designed the methods and analyzed them. CS improved analysis and contributed to discussions and conclusions. MD prepared the manuscript with help from all other co-authors.

Competing Interests

The authors declare that they have no conflict of interest.

Data Availability

The dataset can be found on our Zenodo repository at https://doi.org/10.5281/zenodo.7859851.

Acknowledgements

References

Banwell, A. F., MacAyeal, D. R., and Sergienko, O. V.: Breakup of the Larsen B Ice Shelf triggered by chain reaction drainage of supraglacial lakes, Geophys. Res. Lett., 40, 5872–5876, https://doi.org/10.1002/2013GL057694, 2013.

Bell, R. E., Banwell, A. F., Trusel, L. D., and Kingslake, J.: Antarctic surface hydrology and impacts on ice-sheet mass balance, Nat. Clim. Chang., 8, 1044–1052, https://doi.org/10.1038/s41558-018-0326-3, 2018.

Berthier, E., Scambos, T. A., and Shuman, C. A.: Mass loss of Larsen B tributary glaciers (Antarctic Peninsula) unabated since 2002, Geophys. Res. Lett., 39, https://doi.org/10.1029/2012GL051755, 2012.

Bindschadler, R., Vornberger, P., Fleming, A., Fox, A., Mullins, J., Binnie, D., Paulson, S., Granneman, B., and Gorodetzky, D.: The Landsat Image Mosaic of Antarctica, Remote Sens. Environ., 112, 4214–4226, https://doi.org/10.1016/j.rse.2008.07.006, 2008.

Brucker, L., Picard, G., Arnaud, L., Barnola, J. M., Schneebeli, M., Brunjail, H., Lefebvre, E., and Fily, M.: Modeling time series of microwave brightness temperature at Dome C, Antarctica, using vertically resolved snow temperature and microstructure measurements, J. Glaciol., 57, 171–182, https://doi.org/10.3189/002214311795306736, 2011.

Brun, E.: Investigation on Wet-Snow Metamorphism in Respect of Liquid-Water Content, Ann. Glacial., 13, 22-26. http://doi:10.3189/S0260305500007576, 1989.

Comiso, J. C., Cavalieri, D. J., Parkinson, C. L. and Gloersen, P., Passive microwave algorithms for sea ice concentration: A comparison of two techniques. Remote Sens. Environ., 60, 357-384, 1997.

Durand, M., Kim, E. J. and Margulis, S. A.: Quantifying uncertainty in modeling snow microwave radiance for a mountain snowpack at the point-scale, including stratigraphic effects, IEEE Trans. Geosci. Remote Sens., 46, 1753-1767, 2008.

460   Gelaro, R., McCarty, W., Suárez, M. J., Todling, R., Molod, A., Takacs, L., Randles, C. A., Darmenov, A., Bosilovich, M. G., Reichle, R., Wargan, K., Coy, L., Cullather, R., Draper, C., Akella, S., Buchard, V., Conaty, A., Merkova, D., Nielsen, J. E., Partyka, G., Pawson, S., Putman, W., Rienecker, M., Schubert, S. D., Sienkiewicz, M., & Zhao, B.: The Modern-Era Retrospective Analysis for Research and Applications, Version 2 (MERRA-2), J. Clim., 30, 5419–5454, https://doi.org/10.1175/JCLI-D-16-0758.1, 2017.

465   Haran, T., Klinger, M., Bohlander, J., Fahnestock, M., Painter, T., and Scambos, T.: MEaSUREs MODIS Mosaic of Antarctica 2013-2014 (MOA2014) Image Map, Version 1 [Data Set], Boulder, Colorado USA, NASA National Snow and Ice Data Center Distributed Active Archive Center, https://doi.org/10.5067/RNF17BP824UM, 2018.

Howat, I. M., Porter, C., Smith, B. E., Noh, M.-J., and Morin, P.: The Reference Elevation Model of Antarctica, Cryosphere, 13, 665–674, https://doi.org/10.5194/tc-13-665-2019, 2019.

470   Jakobs, C. L., Reijmer, C. H., Smeets, C. J. P. P., Trusel, L. D., van de Berg, W. J., van den Broeke, M. R., and van Wessem, J. M.: A benchmark dataset of in situ Antarctic surface melt rates and energy balance, J. Glaciol., 66, 291–302, https://doi.org/10.1017/jog.2020.6, 2020.

Kingslake, J., Ely, J. C., Das, I., and Bell, R. E.: Widespread movement of meltwater onto and across Antarctic ice shelves, Nature, 544, 349–352, https://doi.org/10.1038/nature22049, 2017.

475   Lyapustin, A., Tedesco, M., Wang, Y., Aoki, T., Hori, M. and Kokhanovsky, A.: Retrieval of snow grain size over Greenland from MODIS, Remote Sens. Environ., 113, 1976-1987, 2009.

Löwe, H. and Picard, G.: Microwave scattering coefficient of snow in MEMLS and DMRT-ML revisited: the relevance of sticky hard spheres and tomography-based estimates of stickiness, Cryosphere, 9, 2101–2117, https://doi.org/10.5194/tc-9-2101-2015, 2015.

480   Maeda, T., Taniguchi, Y. and Imaoka, K. GCOM-W1 AMSR2 level 1R product: Dataset of brightness temperature modified using the antenna pattern matching technique. IEEE Trans. Geosci. Remote Sens., 54(2), 770-782, 2015.

Mätzler, C.: Relation between grain-size and correlation length of snow, J. Glaciol., 48, 461–466, https://doi.org/10.3189/172756502781831287, 2002.

Picard, G., Fily, M., and Gallee, H.: Surface melting derived from microwave radiometers: A climatic indicator in 485   Antarctica, Ann. Glaciol., 46, 29-34. https://doi:10.3189/172756407782871684, 2007.

Picard, G., Domine, F., Krinner, G., Arnaud, L. and Lefebvre, E. Inhibition of the positive snow-albedo feedback by precipitation in interior Antarctica, Nature Clim. Change, 2, 795–798, https://doi.org/10.1038/nclimate1590, 2012.

Picard, G., Royer, A., Arnaud, L., and Fily, M.: Influence of meter-scale wind-formed features on the variability of the microwave brightness temperature around Dome C in Antarctica, Cryosphere, 8, 1105–1119, https://doi.org/10.5194/tc-8-490   1105-2014, 2014.

Picard, G., Sandells, M., and Löwe, H.: SMRT: an active–passive microwave radiative transfer model for snow with multiple microstructure and scattering formulations (v1.0), Geosci. Model Dev., 11, 2763–2788, https://doi.org/10.5194/gmd-11-2763-2018, 2018.

Picard, G., Leduc-Leballeur, M., Banwell, A. F., Brucker, L., and Macelloni, G.: The sensitivity of satellite microwave 495   observations to liquid water in the Antarctic snowpack, Cryosphere, 16, 5061–5083, https://doi.org/10.5194/tc-16-5061-2022, 2022a.

Picard, G., Löwe, H., Domine, F., Arnaud, L., Larue, F., Favier, V., Le Meur, E., Lefebvre, E., Savarino, J., Royer, A.: The Microwave Snow Grain Size: A New Concept to Predict Satellite Observations Over Snow-Covered Regions, AGU Adv., 3(4), https://doi.org/10.1029/2021AV000630, 2022b.

500   Proksch, M., Löwe, H., and Schneebeli, M.: Density, specific surface area, and correlation length of snow measured by high-resolution penetrometry, J. Geophys. Res. Earth Surf., 120, 346–362, https://doi.org/10.1002/2014JF003266, 2015.

Rignot, E.: Accelerated ice discharge from the Antarctic Peninsula following the collapse of Larsen B ice shelf, Geophys. Res. Lett., 31, L18401, https://doi.org/10.1029/2004GL020697, 2004.

Roy, A., Picard, G., Royer, A., Montpetit, B., Dupont, F., Langlois, A., Derksen, C., and Champollion, N.: Brightness 505   Temperature Simulations of the Canadian Seasonal Snowpack Driven by Measurements of the Snow Specific Surface Area, IEEE Trans. Geosci. Remote Sens., 51, 4692–4704, https://doi.org/10.1109/TGRS.2012.2235842, 2013.

Scambos, T. A., Hulbe, C., Fahnestock, M., and Bohlander, J.: The link between climate warming and break-up of ice shelves in the Antarctic Peninsula, J. Glaciol., 46, 516–530, https://doi.org/10.3189/172756500781833043, 2000.

Scambos, T., Haran, T., Fahnestock, M., Painter, T., and Bohlander, J.: MODIS-based Mosaic of Antarctica (MOA) data sets: 510   Continent-wide   surface   morphology   and   snow   grain   size, Remote   Sensing   of   Environment, 111, http://doi:10.1016/j.rse.2006.12.020, 2007.

Stevens, C. M., Verjans, V., Lundin, J. M. D., Kahle, E. C., Horlings, A. N., Horlings, B. I., and Waddington, E. D.: The Community Firn Model (CFM) v1.0, Geosci. Model Dev., 13, 4355–4377, https://doi.org/10.5194/gmd-13-4355-2020, 2020.

Tikhonov, V. V., Raev, M. D., Khvostov, I. V., Boyarskii, D. A., Romanov, A. N., Sharkov, E. A., and Komarova, N. Yu.: 515   Analysis of the Seasonal Dependence of the Brightness Temperature of the Glacier Sheet of Antarctica by Microwave Satellite Data, Izv. Atmos. Ocean. Phys., 55, 1302–1313, https://doi.org/10.1134/S0001433819090512, 2019.

Torinesi, O., Fily, M., and Genthon, C.: Variability and Trends of the Summer Melt Period of Antarctic Ice Margins since 1980   from   Microwave   Sensors,   J.   Clim.,   16,   1047–1060,   https://doi.org/10.1175/1520-0442(2003)016<1047:VATOTS>2.0.CO;2, 2003.

520   Zwally, J. H. and Fiegles, S.: Extent and duration of Antarctic surface melting, J. Glaciol., 40, 463–475, https://doi.org/10.3189/S0022143000012338, 1994.

525
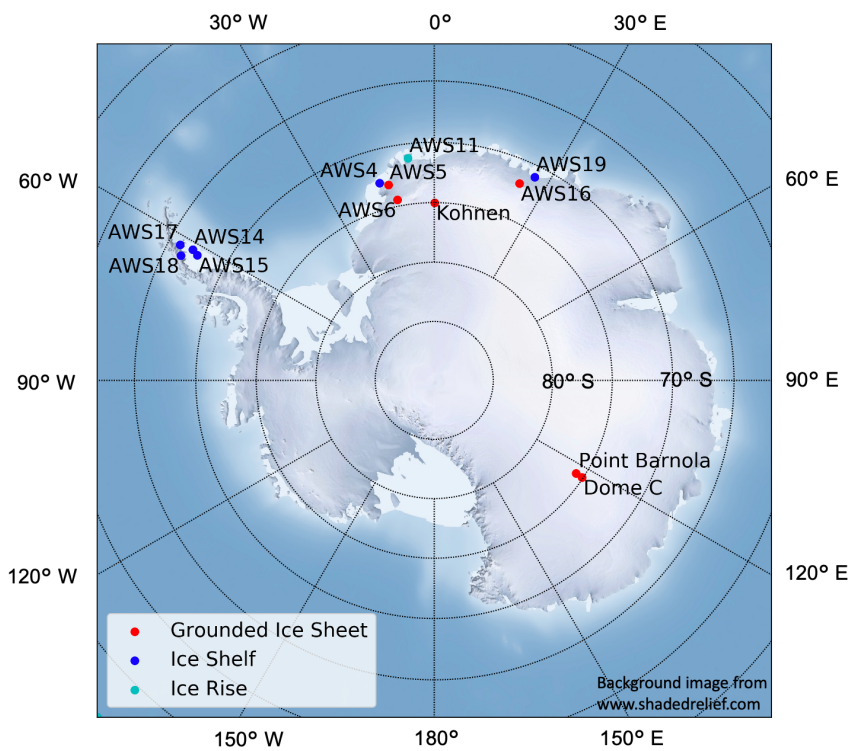
Figure 1: The thirteen AIS point locations that are used in this study. Sites on grounded ice sheet are red, sites on ice shelves are blue, and sites on ice rises are cyan. Background image from www.shadedrelief.com.
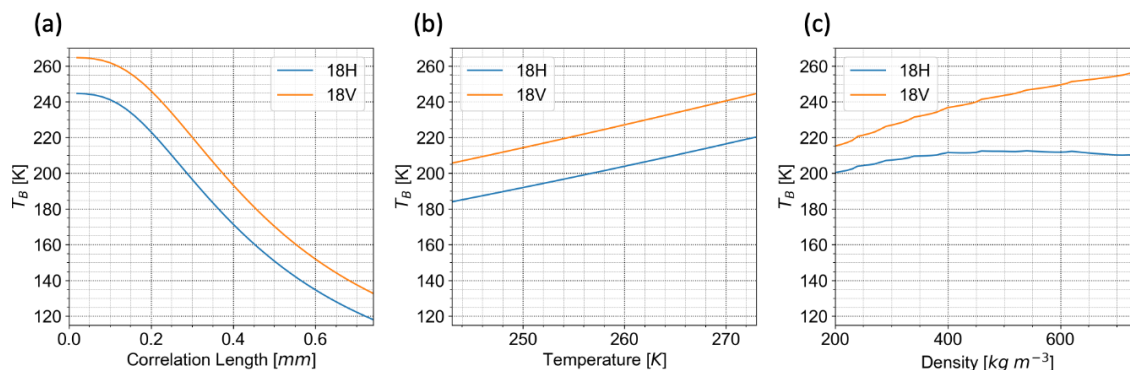
Figure 2: (a) Holding temperature and density constant (at 265 K and 375 kg m⁻³), the blue and orange lines show how brightness temperature varies with respect to correlation length for 18H and 18V, respectively. (b) Holding correlation length and density constant (at 0.25 mm and 375 kg m⁻³), the blue and orange lines show how brightness temperature varies with respect to temperature for 18H and 18V, respectively. (c) Holding correlation length and temperature constant (at 0.25 mm and 265 K), the blue and orange lines show how brightness temperature varies with respect to density for 18H and 18V, respectively.
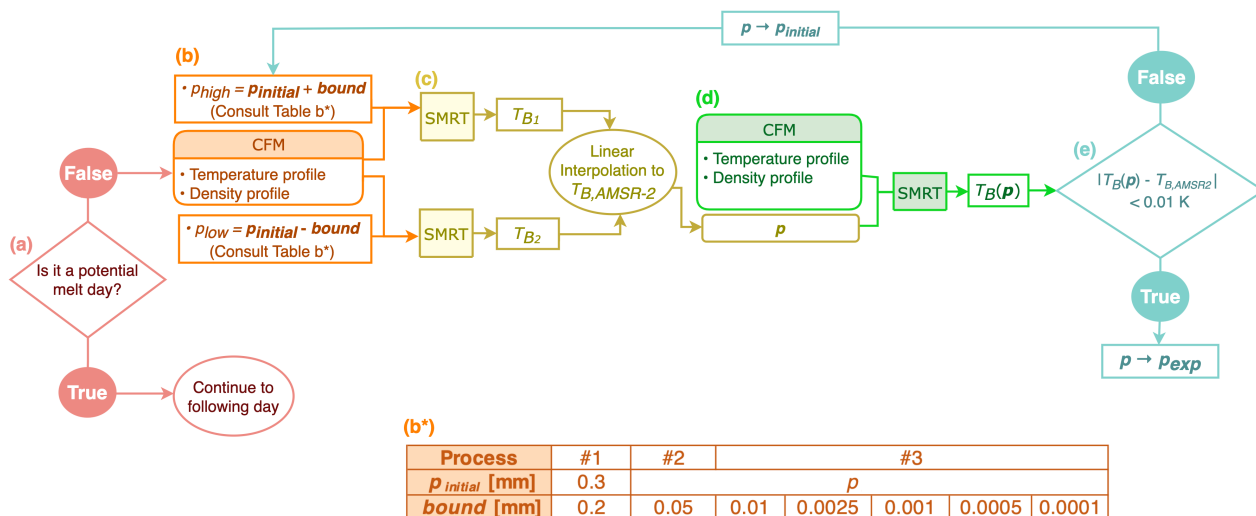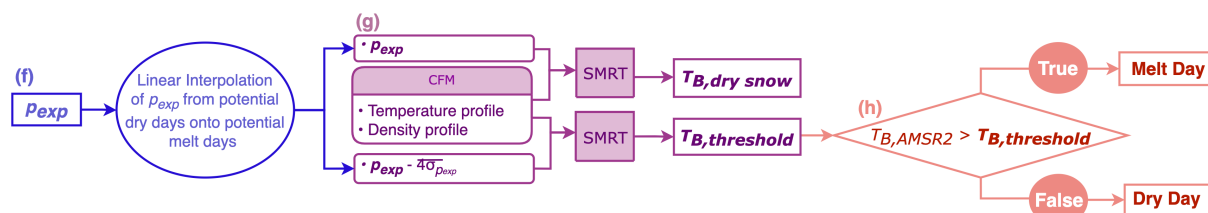
Figure 3: Flow chart showing the hybrid-method algorithm used to calculate melt days. Step 1 (top) illustrates how correlation length (p_{exp}) is calculated using CFM and SMRT using repeated linear interpolations. Step 2 (bottom) illustrates how brightness temperature ($T_{B, dry\ snow}$) and its dynamic threshold ($T_{B,threshold}$) can then be calculated from p_{exp}, and used to determine melt days versus dry days. (a-h) are individual steps described in the main text.
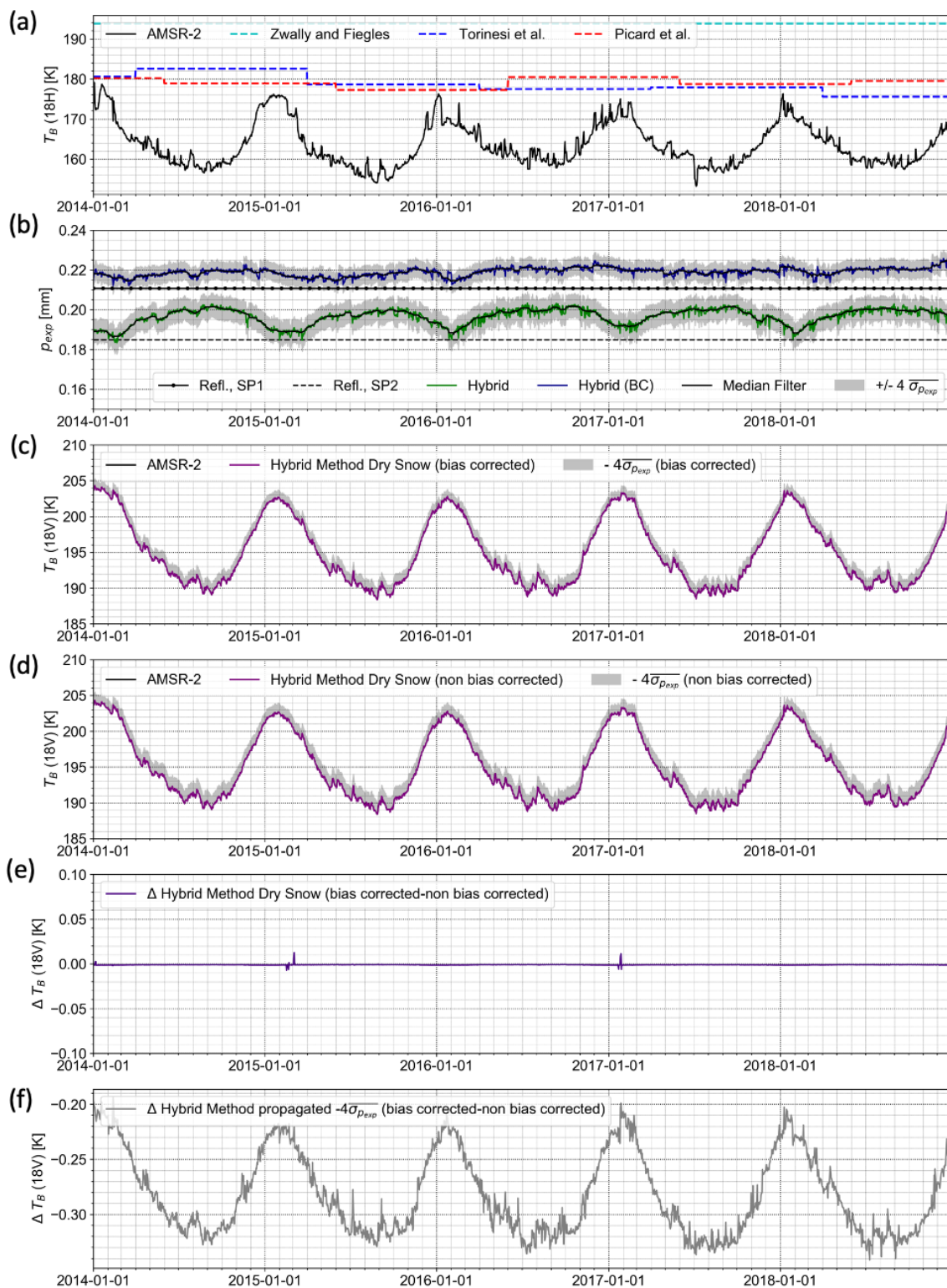
540

Figure 4: Dome C (a) Brightness temperature from AMSR-2 (18H; black line) with thresholding techniques from Zwally and Fiegles (1994; cyan line), Torinesi et al. (2003; blue line), and Picard et al. (2022a; red line). (b) Correlation length converted from NIR SSA values in Brucker et al. (2011) assuming a 4 m penetration depth (black dotted line) and a 10 m penetration depth (black dashed line). Correlation length computed from the hybrid method (18H; green line) and the hybrid method BC version (navy line) along

550 **with grey bounds that represent $4\overline{\sigma_{p_{exp}}}$. (c) AMSR-2 brightness temperature (18V; black line). Hybrid method dry snow brightness temperature, BC version (18V; purple line) along with propagated $4\overline{\sigma_{p_{exp}}}$. (d) Same as (c) but for non-BC version. (e) The difference between the hybrid method's dry snow brightness temperature BC and non-BC versions (18V; purple line). (f) The difference between propagated $4\overline{\sigma_{p_{exp}}}$ between the BC and non-BC versions (grey line).**

555
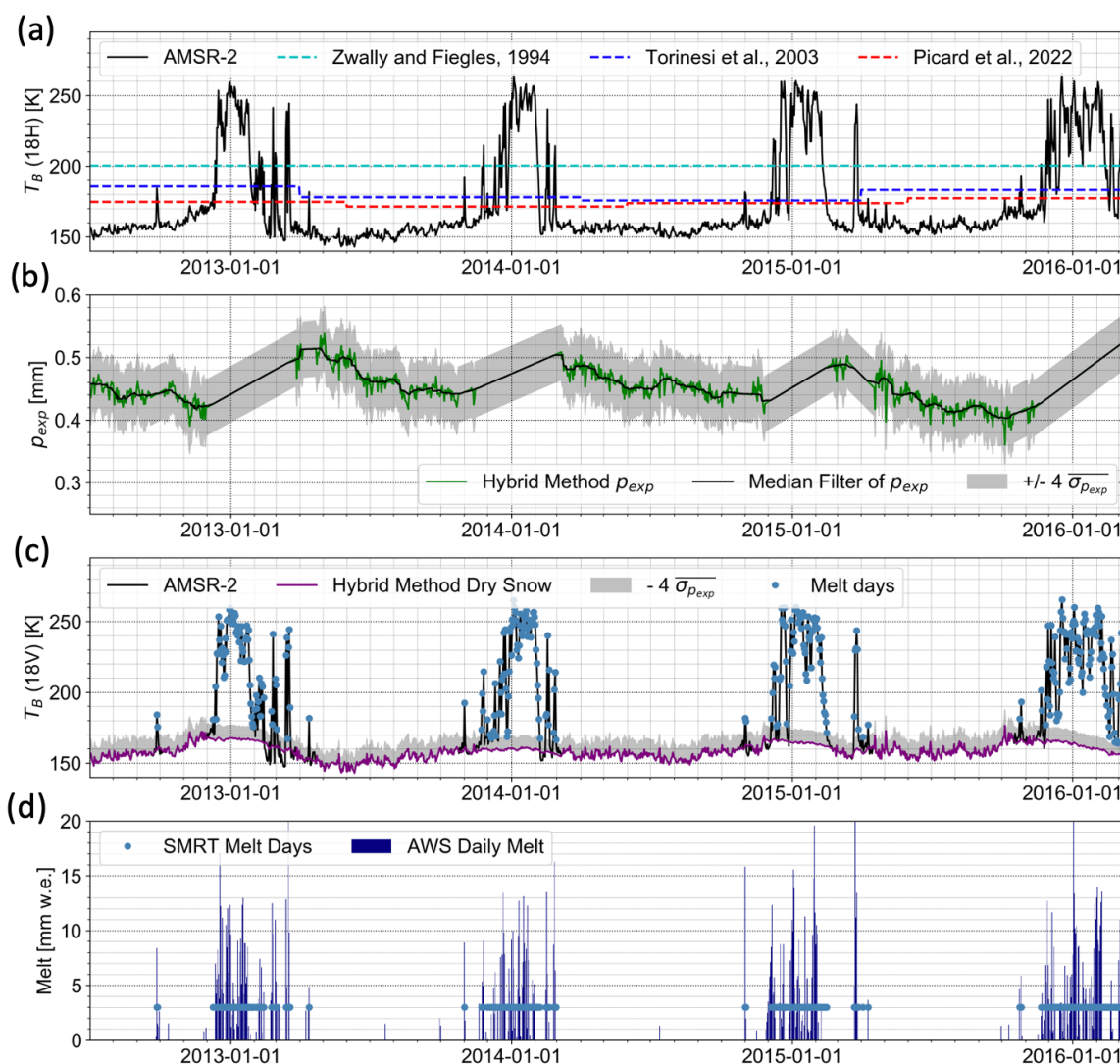
Figure 5: Data from AWS 17 (a) Brightness temperature from 18H from AMSR-2 (black line) with thresholding techniques from Zwally and Fiegles (1994; cyan line), Torinesi et al. (2003; blue line), and Picard et al. (2022a; red line). (b) The exponential correlation length computed from the hybrid method (18H; green line) along with +/- $4\overline{\sigma_{p_{exp}}}$ bounds, with median filter (black line). (c) AMSR-2 brightness temperature (18H; black line). Hybrid method dry snow brightness temperature (18H; purple line) with
560 **propagated $4\overline{\sigma_{p_{exp}}}$ (grey bounds). Melt days detected by hybrid method (blue dots). (d) Melt days detected by hybrid method (blue dots). These represent melt days versus dry days in a binary fashion and do not reflect a specific melt volume. AWS surface energy balance melt data (dark blue bars).**
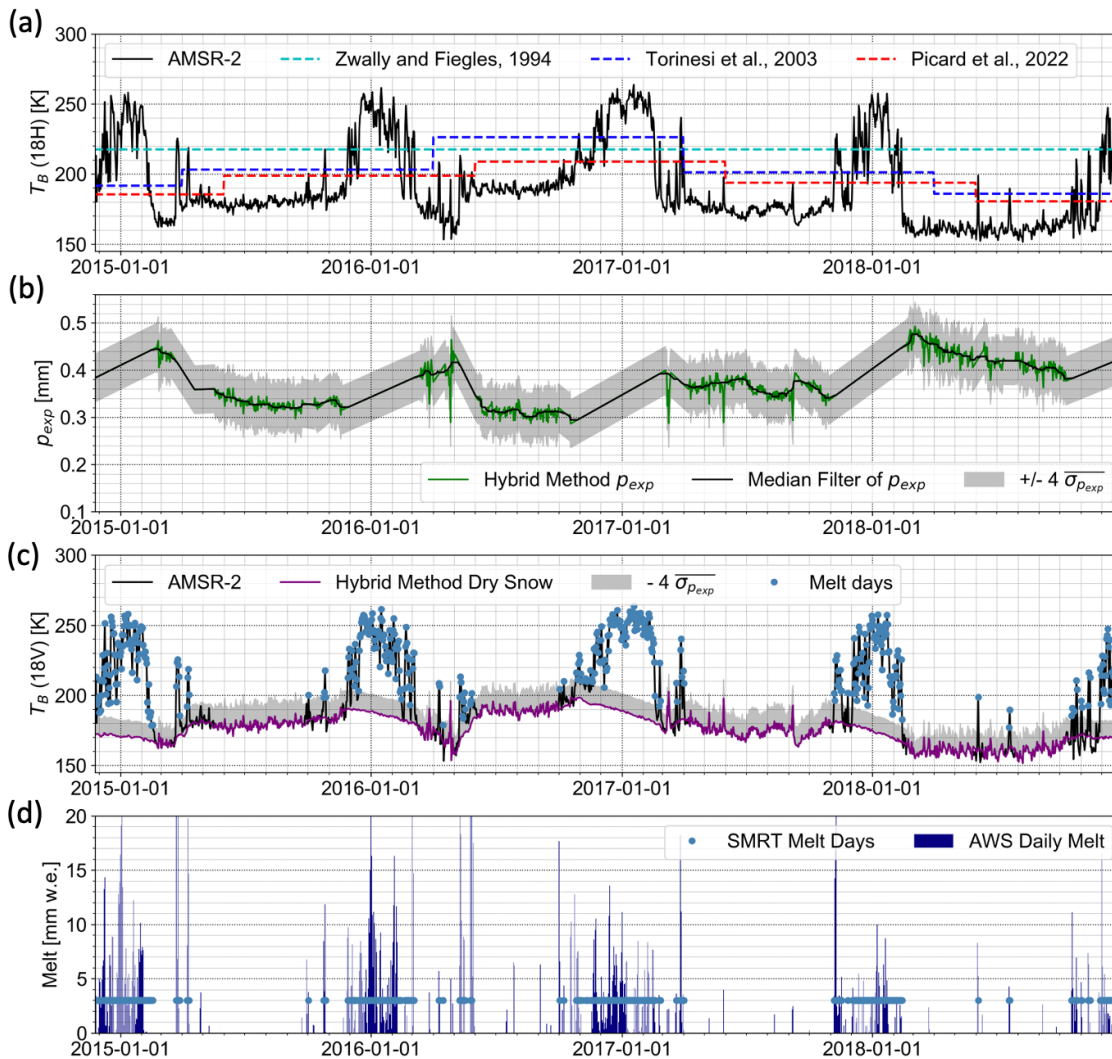

Figure 6: Data from AWS 18 (a) Brightness temperature from 18H from AMSR-2 (black line) with thresholding techniques from
565 **Zwally and Fiegles (1994; cyan line), Torinesi et al. (2003; blue line), and Picard et al. (2022a; red line). (b) The exponential correlation length computed from the hybrid method (green line) along with +/- $4\overline{\sigma_{p_{exp}}}$ bounds, with median filter (black line). (c)**

AMSR-2 brightness temperature (18H; black line). Hybrid method dry snow brightness temperature (18H; purple line) with propagated $4\overline{\sigma_{p_{exp}}}$ (grey bounds). Melt days detected by hybrid method (blue dots). (d) Melt days detected by hybrid method (blue dots). AWS surface energy balance melt data (dark blue bars).
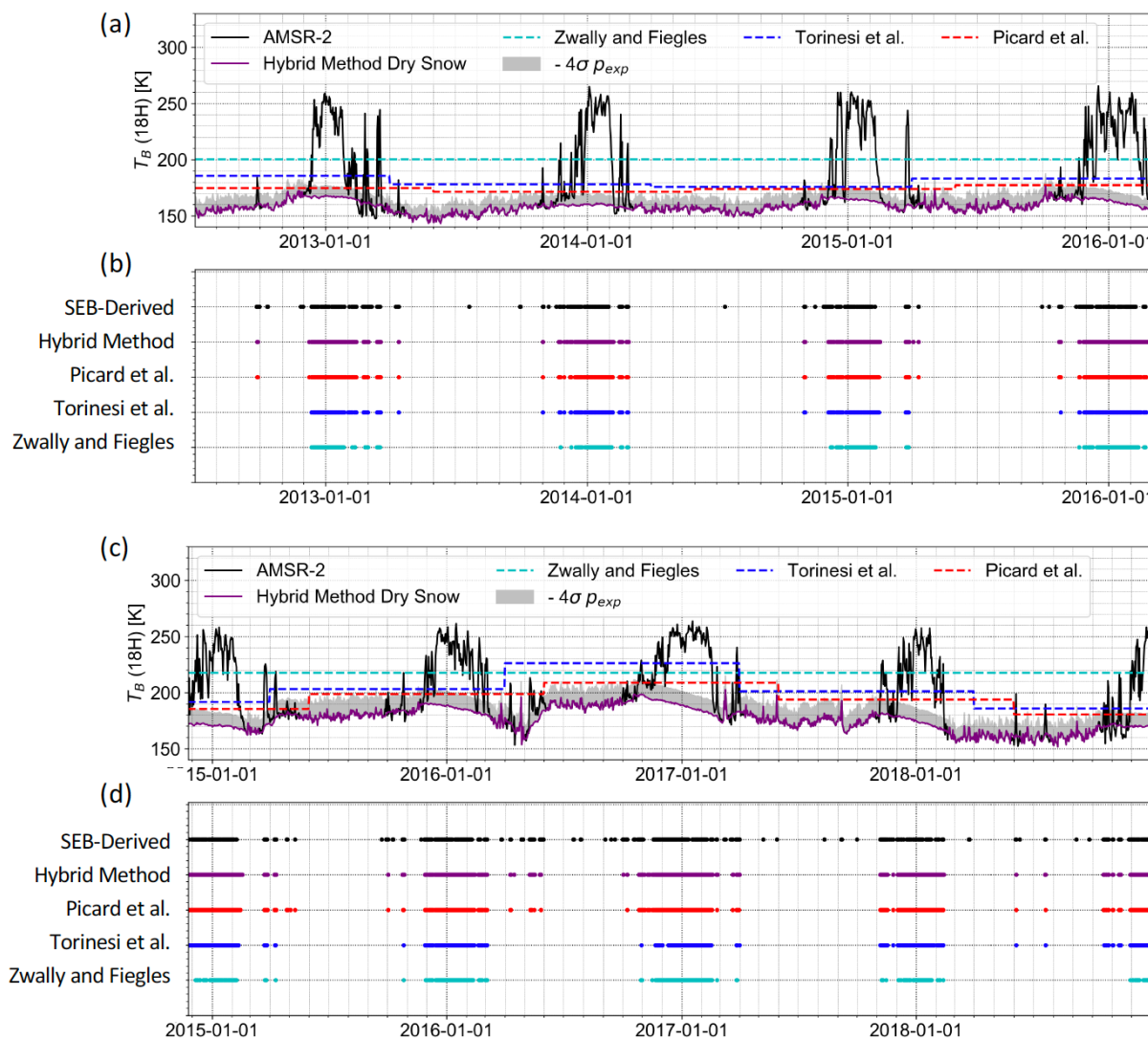
570

Figure 7: Results for AWS 17 (a & b) and AWS 18 (c & d). (a & c) Brightness temperature from 18H with thresholding techniques from Zwally and Fiegles (1994; cyan line), Torinesi et al. (2003; blue line), and Picard et al. (2022a; red line). Hybrid method dry snow brightness temperature (18H; purple line) with propagated $4\overline{\sigma_{p_{exp}}}$ (grey bounds). (b & d) Days when AWS surface energy balance melt > 0 (black dots). Melt days detected by hybrid method (purple dots). Melt days detected by Picard et al. (2022a; red dots), Torinesi et al., (2003; blue dots), and Zwally and Fiegles (1994; cyan dots).

23

AWS17	# Days	% Melt Days	Matching days/ Total days	Mismatched dry days/ Total days	Mismatched melt days/ Total days
Observations	2525	20.7%	N/A	N/A	N/A
Hybrid Method	2525	24.2%	90.9%	3.0%	6.2%
Picard et al.	2525	22.4%	91.7%	3.3%	5.0%
Torinesi et al.	2525	20.9%	91.7%	4.0%	4.3%
Zwally & Fiegles	2525	16.4%	90.9%	6.3%	2.7%
AWS18	# Days	% Melt Days	Matching days/ Total days	Mismatched dry days/ Total days	Mismatched melt days/ Total days
Observations	1977	27.2%	N/A	N/A	N/A
Hybrid Method	1977	27.8%	89.2%	4.1%	6.7%
Picard et al.	1977	26.3%	89.3%	4.7%	6.0%
Torinesi et al.	1977	23.2%	87.4%	7.6%	4.9%
Zwally & Fiegles	1977	18.3%	86.4%	10.5%	3.1%

580 **Table 1: A table comparing the hybrid method, Picard et al. (2022a), Torinesi et al. (2003), and Zwally and Fiegles (1994) methods of melt day detection for AWS 17 and AWS 18 to SEB-derived melt data. "Matching days" refers to the sum of both melt and dry days that match with SEB-derived melt data. "Mismatched dry days" refers to days when a technique identifies a dry day when that day is considered melt by SEB-derived melt data. "Mismatched melt days" refers to days when a technique identifies a melt day when that day is considered dry by SEB-derived melt data.**

585

590

The Cryosphere
Discussions
Open Access

EGU
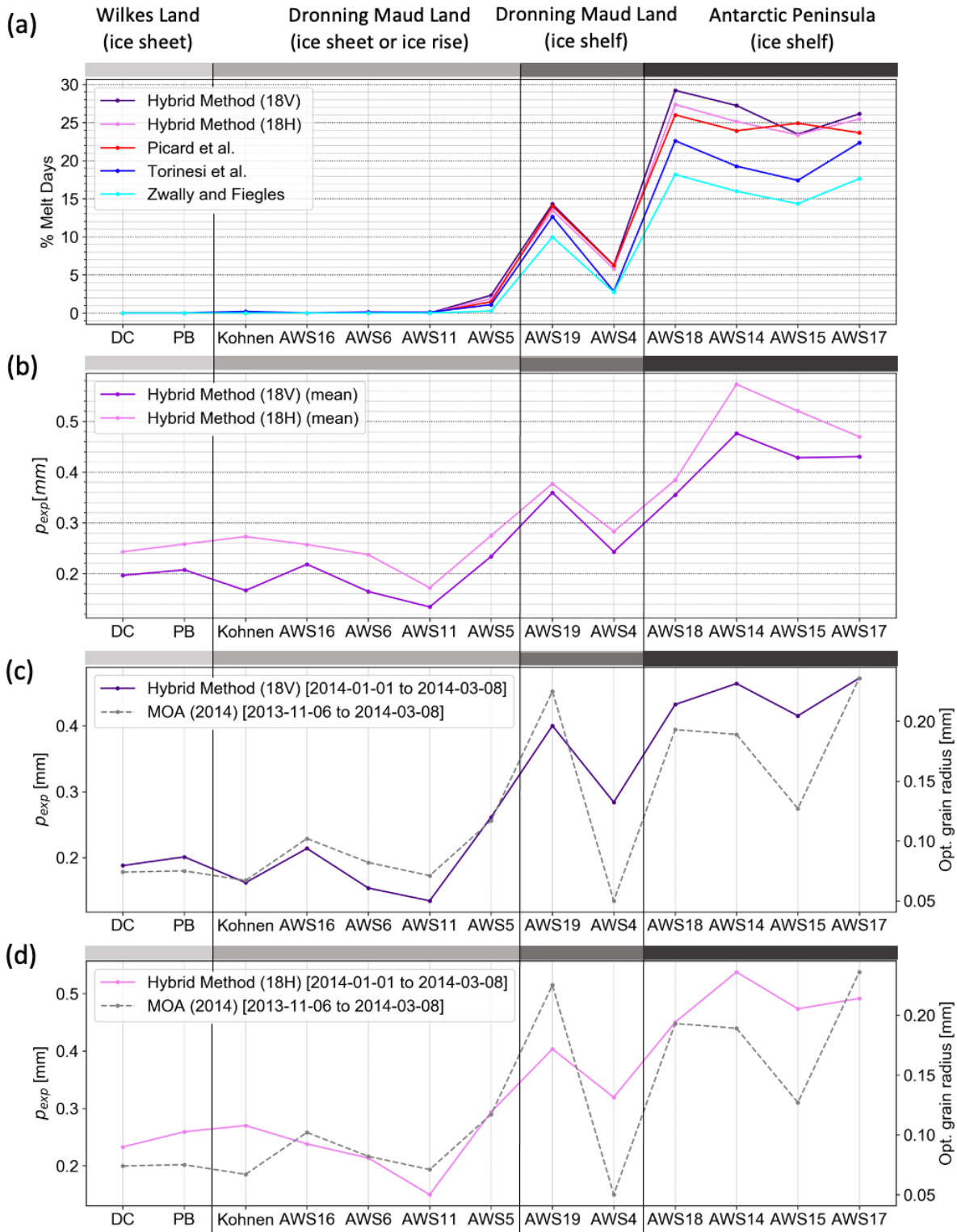
Figure 8: Sites are divided with vertical black lines by region. (a) Percentage of the days from the beginning of 2014 to the end of 2018 that are assigned melt using the Hybrid Method (18V; purple line), Hybrid Method (18H; pink line), Picard et al. (2022a; red line), Torinesi et al. (2003; blue line), and Zwally and Fiegles (1994; cyan line). (b) Mean correlation length ($\overline{p_{exp}}$) across this time series using the Hybrid Method at the 18V channel (purple line) and 18H channel (pink line). (c & d) Hybrid method correlation

600   **length data from January 1st, 2014 to March 8th 2018 for 18V (c; purple line) and 18H (d; pink line). Compared to optical grain size from MEaSUREs MODIS Mosiac of Antarctica in 2014 (grey dashed line; Scambos et al., 2007; Haran et al., 2018).**
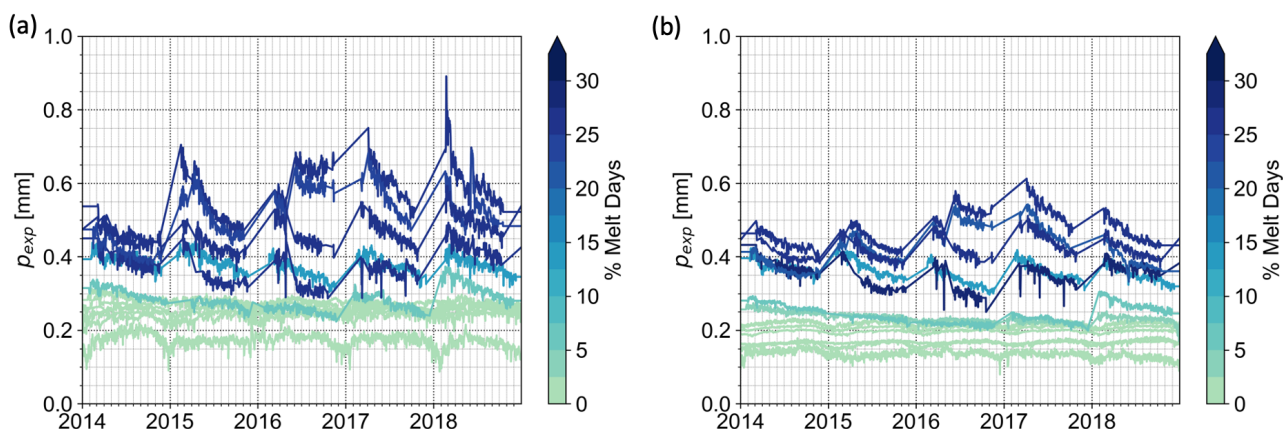

Figure 9: Correlation length for all sites colored by the percentage of the days in the time series that are assigned melt using (a) the 18H AMSR-2 channel and (b) the 18V AMSR-2 channel.

605